

High Responsivity, Large-Area Graphene/MoS₂ Flexible Photodetectors

D. De Fazio¹, I. Goykhman¹, M. Bruna¹, A. Eiden¹, S. Milana¹, D. Yoon¹, U. Sassi¹, M. Barbone¹, D. Dumcenco², K. Marinov², A. Kis², and A. C. Ferrari^{1*}
¹Cambridge Graphene Centre, University of Cambridge, Cambridge CB3 0FA, UK and
²Electrical Engineering Institute, Ecole Polytechnique Federale de Lausanne, Switzerland

We present flexible photodetectors (PDs) for visible wavelengths fabricated by stacking centimetre-scale chemical vapor deposited (CVD) single layer graphene (SLG) and single layer CVD MoS₂, both wet transferred onto a flexible polyethylene terephthalate substrate. The operation mechanism relies on injection of photoexcited electrons from MoS₂ to the SLG channel. The external responsivity is 45.5A/W and the internal 570A/W at 642nm. This is at least two orders of magnitude higher than bulk-semiconductor flexible membranes and other flexible PDs based on graphene and layered materials. The photoconductive gain is up to 4×10^5 . The photocurrent is in the 0.1-100 μ A range. The devices are semi-transparent, with just 8% absorption at 642nm and work stably upon bending to a curvature of 6cm. These capabilities and the low voltage operation (< 1V) make them attractive for wearable applications.

INTRODUCTION

Modern electronic and opto-electronic systems such as smart phones, smart glasses, smart watches, wearable devices and electronic tattoos increasingly require ultra-thin, transparent, low-cost and energy efficient devices on flexible substrates[1]. The rising demand for flexible electronics and optoelectronics requires materials which can provide a variety of electrical and optical functionalities, with constant performance upon application of strain[2]. A wide range of optoelectronic devices on flexible substrates have been reported to date, such as photodetectors (PDs)[3, 4], light emitting diodes (LEDs)[5], optical filters[6], optical interconnects[7, 8], photovoltaic devices[9, 10] and biomedical sensors[11, 12].

Major challenges in the development of flexible optoelectronic devices stem from the limitations associated with the high stiffness of bulk semiconductors[13, 14]. In the case of flexible PDs, the current approaches primarily rely on thin (μ m-thick) semiconductor membranes[4, 15] and compound semiconductor nanowires (NWs)[3, 16–18], mainly because of their ability to absorb light throughout the whole visible range (0.4-0.7 μ m) and the possibility to adapt their fabrication techniques from rigid to plastic, or deformable substrates[1].

One of the key parameters for PDs characterization is the responsivity. This is defined as the ratio between the collected photocurrent (I_{ph}) and the optical power. The responsivity is named external ($R_{ext} = I_{ph}/P_o$)[19] or internal ($R_{int} = I_{ph}/P_{abs}$)[19], whenever the incident (P_o) or absorbed (P_{abs}) optical power is used at the denominator. Since not all incident photons are absorbed, i.e. $P_{abs} < P_{in}$, then R_{int} is typically larger than R_{ext} [19].

In flexible PDs, R_{ext} up to $\sim 0.3A/W$ was reported for crystalline semiconductor membranes (InP, Ge)[4, 15] with integrated p-i-n junctions, showing photocurrent up to $\sim 100\mu A$, with $\sim 30\%$ degradation upon bending at a radius $r_b \sim 3cm$ [15]. PDs made of a single semiconductor NW on flexible substrates[3, 16–18] demonstrated R_{ext}

up to $\sim 10^5 A/W$, for r_b down to 0.3cm[3]. Yet, these provide limited I_{ph} in the order of nA [3, 16, 18] up to less than $1\mu A$ [17]. For flexible devices exploiting NW-arrays by drop-casting[3, 16, 18], rather than based on single-NWs, R_{ext} degrades significantly from $\sim 10^5 A/W$ to the mA/W range[3, 16, 18], due to photocurrent loss at multiple junctions in the NW network[3, 16, 18].

Graphene and related materials (GRMs) have great potential in photonics and optoelectronics[20–23]. A variety of GRM-based devices have been reported, such as flexible displays[24], photovoltaic modules[25, 26], photodetectors[22, 27, 28], optical modulators[29], plasmonic devices[30–34], and ultra-fast lasers[23]. Heterostructures, obtained by stacking layers of different materials were also explored[21, 22], e.g. in photovoltaic[35] and light emitting devices[36]. Refs.37, 38 reported SLG/MoS₂-based PDs made of mechanically exfoliated[37] or CVD grown[38] materials, transferred on Si/SiO₂ rigid substrates. These reached back-gate dependent $R_{int} \sim 10^8 A/W$ for optical intensities $< 0.1pW/\mu m^2$.

GRM based flexible PDs have been reported for visible light (0.4 – 0.7 μm [39, 40]) using materials produced by liquid phase exfoliation (LPE)[41, 42] of graphene and transition metal dichalcogenides (TMDs)[39, 40]. In Ref.40, a flexible PD on polyethylene terephthalate (PET) was fabricated by sandwiching a LPE dispersion of WS₂ between a LPE graphene film serving as a back electrode and a chemical vapor deposited (CVD) graphene top electrode, with $R_{ext} \sim 0.1mA/W$. This value is orders of magnitude lower compared to other flexible PDs[3, 4, 15–18]. The lower R_{ext} in LPE-based devices is attributed to non-efficient inter-flake charge transfer[43, 44], resulting in limited conductivity[43, 44] and poor collection of photo-generated carriers at the outer metal electrodes[40]. Similarly, the inefficient charge transfer affected R_{ext} (in the nA/W range) in Ref.39, where a PD was fabricated with LPE MoS₂ as absorber and LPE graphene as top electrode.

Here we take advantage of the mechanical properties of

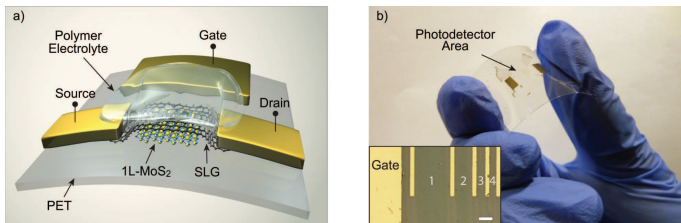


FIG. 1: a) Schematic SLG/MoS₂ flexible PD, side-gated with a polymer electrolyte. b) Picture of a typical PD, showing transparency and flexibility. (Inset) Optical image of 4 PDs with different channel lengths and common side gate electrode. Scale bar is 200 μ m.

layered materials to demonstrate flexible gate-controlled SLG/MoS₂ PDs for visible wavelengths with R_{ext} of tens of A/W and optical transparency > 80%. The devices are assembled by stacking on a PET substrate a centimetre-scale CVD SLG on a CVD-grown single layer MoS₂ (1L-MoS₂). In this configuration, 1L-MoS₂ acts as visible light absorber, while SLG is the conductive channel for I_{ph} flow[37, 38]. We show that R_{ext} increases either by promoting carrier injection from 1L-MoS₂ to SLG using polymer electrolyte gating, or by increasing the source-drain voltage. We get R_{ext} up to ~ 45 A/W applying a 1V bias with $I_{ph} \sim$ tens μ A. These values are at least two orders of magnitude higher than those reported in semiconductor membranes devices[4, 15], semiconductor NW arrays[3, 16–18] and GRM-based[39, 40] flexible PDs operating in the visible range[3, 4, 15–18, 39, 40]. This R_{ext} is achieved in devices with $\sim 82\%$ transparency, twice that reported for semiconductor membrane devices[15]. We get $R_{int} \sim 570$ A/W for ~ 0.1 nW/ μ m² at 642nm, similar to SLG/MoS₂ PDs[37, 38] on rigid substrate operating at the same optical power level. This shows that SLG/MoS₂ heterostructures on PET retain their photodetection capabilities. Upon bending, our devices have stable performance for r_b down to ~ 6 cm. This is comparable to r_b measured in semiconductor membranes PDs[4, 15], which show lower (< 0.3 A/W) responsivities[4, 15]. Although our r_b is one order of magnitude larger than for flexible single NWs[3, 16–18], the latter had at least three orders of magnitude smaller device areas ($< 5\mu$ m²)[3, 16–18] compared to our PDs (> 0.2 mm²). Given the responsivity, flexibility, transparency and low operation voltage (below 1V), our PDs may be integrated in wearable, biomedical and low-power opto-electronic applications[11, 12, 17].

RESULTS AND DISCUSSION

Fig.1 plots a schematic drawing of our PD. The device consists of a 1L-MoS₂ absorber covered by a SLG channel, clamped between source and drain electrodes. We chose PET as a flexible substrate due to its $\sim 90\%$

transparency in the visible range[45] and ability to withstand solvents[46] (e.g acetone and isopropyl alcohol) commonly used in the transfer processes of 2d materials grown by CVD (e.g. transfer of SLG grown on Cu)[47]. The SLG/1L-MoS₂ heterostructure is gated using a polymer electrolyte[48, 49].

The operation principle of our devices is depicted in Fig.2. For energy bands alignment, the electron affinity of 1L-MoS₂ and the Dirac point of SLG are assumed to be ~ 4.4 eV[50, 51] and ~ 4.6 eV[52, 53], respectively. We also assume SLG to be initially p-doped (Fig.2a), as reported in previous works involving SLG transferred on PET substrates[54, 55]. In thermodynamic equilibrium, E_F is constant across the device and is located below the Dirac point. During illumination, part of the photo-generated electrons would be injected from the 1L-MoS₂ conduction band into the p-doped SLG[37, 38], leaving behind uncompensated photogenerated holes. The latter would act as an additional positive V_{GS} to the SLG channel, seen as a shift of the charge neutrality point (V_{CNP}) to more negative voltages. In p-doped SLG, the injected electrons from 1L-MoS₂ would occupy energy states above E_F (Fig.2b), thus reducing the concentration of holes and decreasing the PD current. Electron injection can be further promoted by gating. When negative V_{GS} is applied, higher p-doping of the SLG channel would induce a stronger electric field at the SLG/1L-MoS₂ interface[38], thus favoring electron transfer from 1L-MoS₂ (Fig.2b). Hence, for negative V_{GS} , R_{ext} is expected to increase, due to injection of more electrons and consequent more pronounced PD current reduction. The opposite should happen for positive V_{GS} , where the gate-induced negative charge in SLG would reduce the p-doping and shift E_F towards the Dirac point. In this case, the photogenerated electrons in 1L-MoS₂ would experience weaker electric fields, becoming less attracted by the SLG channel. As a result, we expect R_{ext} to decrease. When positive V_{GS} is high enough, E_F would cross the Dirac point and SLG would become n-doped (Fig.2c). Thus, only weak electron injection from 1L-MoS₂ would be possible if E_F in SLG remains below the 1L-MoS₂ conduction band; the transferred electrons increase free-carriers concentration in the n-doped channel, hence minor increments of R_{ext} and I_{ph} are expected.

Our devices are built as follows. 1L-MoS₂ is epitaxially grown by CVD on c-plane sapphire substrates[56]. These are annealed at 1000 $^{\circ}$ C in air for 1 hour after consecutive cleaning by acetone/isopropyl alcohol/deionized (DI) water. They are then placed face-down above a crucible containing ~ 5 mg MoO₃ ($\geq 99.998\%$ Alfa Aesar). This is loaded into a 32mm outer diameter quartz tube placed in a split-tube three-zone furnace. A second crucible containing 350mg sulfur ($\geq 99.99\%$ purity, Sigma Aldrich) is located upstream from the growth substrates. Ultrahigh-purity Ar is used as carrier gas at atmospheric pressure. The procedure is: ramp the temperature to 300 $^{\circ}$ C with

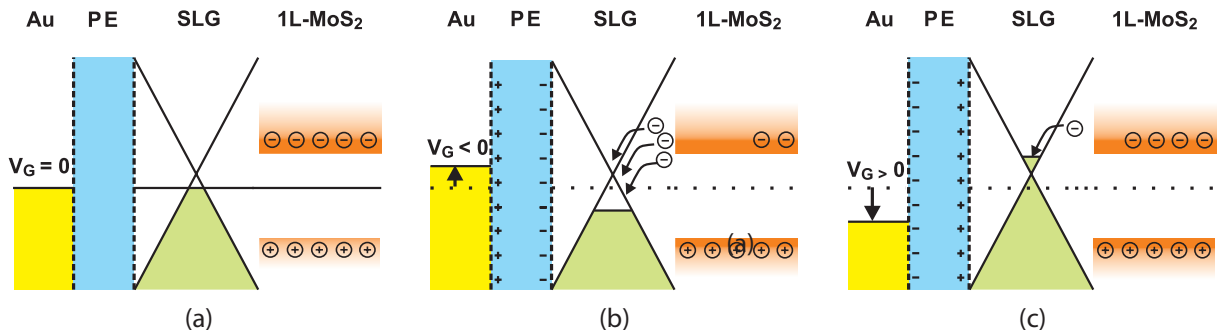


FIG. 2: Schematic band diagram of polymer electrolyte (PE) gated SLG/1L-MoS₂ PD at a) zero, b) negative, c) positive V_{GS}

200sccm Ar flow, set to 300°C for 10mins, ramp to 700°C (50°C/min increase temperature rate) with 10sccm Ar flow, set at 700°C for 10 min, cool to 570°C with 10sccm of Ar, increase the gas flow to 200sccm and open the furnace for rapid cooling[56]. SLG is grown on 35 μ m Cu foil, following the process described in Ref.47. The substrate is annealed in hydrogen atmosphere (H₂, 20sccm) up to 1000°C for 30 minutes. Then, 5sccm CH₄ is added to initiate growth[47, 57]. The sample is then cooled in vacuum (1mTorr) to room temperature and removed from the chamber.

Prior to assembling the SLG/MoS₂ stack, the quality and uniformity of MoS₂ on sapphire and SLG on Cu are inspected by Raman spectroscopy and photoluminescence (PL), using a Horiba Jobin Yvon HR800 spectrometer equipped with a 100X objective. The laser power is kept below 100 μ W (spot size < 1 μ m in diameter) to avoid possible heating effects or damage. Fig.3a (green curve) plots the Raman spectrum of CVD MoS₂ on sapphire for 514nm excitation. The peak at $\sim 385\text{cm}^{-1}$ corresponds to the in-plane (E_{2g}^1) mode[58, 59], while that at $\sim 404\text{cm}^{-1}$, is the out of plane (A_{1g}) mode[58, 59], with full width at half maximum $\text{FWHM}(E_{2g}^1)=2.5$ and $\text{FWHM}(A_{1g})=3.6\text{cm}^{-1}$, respectively. The E_{2g}^1 mode softens, whereas the A_{1g} stiffens with increasing layer thickness[60, 61], so that their frequency difference can be used to monitor the number of layers[60]. The peak position difference $\sim 20\text{cm}^{-1}$ is an indicator of 1L-MoS₂[60]. The peak at $\sim 417\text{cm}^{-1}$ (marked by asterisk in Fig.3a) corresponds to the A_{1g} mode of sapphire[62].

The Raman spectrum measured at 514 nm of SLG on Cu is shown in Fig.3b (magenta curve). This is obtained after the removal of the non-flat background PL of Cu[63]. The two most intense features are the G and the 2D peak, with no significant D peak. The G peak corresponds to the E_{2g} phonon at the Brillouin zone centre[66]. The D peak is due to the breathing modes of sp^2 rings and requires a defect for its activation by double resonance[64–67]. The 2D peak is the second order of the D peak[66]. This is always seen, even when no D peak is present, since no defects are required for the activation of two phonons with the same

momentum, one backscattering from the other[66]. In our sample, the 2D peak is a single sharp Lorentzian with $\text{FWHM}(2D)\sim 26\text{cm}^{-1}$, a signature of SLG[64]. Different (~ 20) measurements show similar spectra, indicating uniform quality. The position of the G peak, $\text{Pos}(G)$, is $\sim 1589\text{cm}^{-1}$, with $\text{FWHM}(G)\sim 13\text{cm}^{-1}$. The 2D peak position, $\text{Pos}(2D)$ is $\sim 2698\text{cm}^{-1}$, while the 2D to G peak intensity and area ratios, $I(2D)/I(G)$ and $A(2D)/A(G)$, are 2.6 and 5.8, respectively, indicating a p-doping $\sim 300\text{meV}$ [48, 68, 69], which corresponds to a carrier concentration $\sim 5 \cdot 10^{12}\text{cm}^{-2}$.

Another evidence for 1L-MoS₂ comes from the PL spectrum [Fig.4a (green curve)], showing a peak $\sim 658\text{nm}$ ($\sim 1.88\text{eV}$), due to band-to-band radiative recombination of electron-hole pairs in 1L-MoS₂[70].

Then, the MoS₂ film is transferred onto a PET substrate from sapphire using a KOH-based approach[56]. The samples are first spin coated with $\sim 100\text{nm}$ poly-methyl methacrylate (PMMA). This is detached in a 30% KOH solution, washed in DI water and transferred onto PET. The PMMA is then dissolved in acetone. Subsequently, SLG is transferred on the 1L-MoS₂ on PET. PMMA is spin coated on the SLG/Cu substrate, then placed in a solution of ammonium persulfate (APS) in DI water until Cu is etched[41, 47]. The PMMA membrane with attached SLG is then transferred to a beaker filled with DI water for cleaning APS residuals. The membrane is subsequently lifted with the target PET substrate having 1L-MoS₂ on top. After drying, PMMA is removed in acetone leaving SLG on 1L-MoS₂.

Raman and PL characterizations are performed at each step of the SLG/1L-MoS₂ assembly on PET, i.e on 1L-MoS₂ transferred on PET, and on SLG on 1L-MoS₂. This is to confirm no degradation during the fabrication process. For 1L-MoS₂ on PET, the Raman at 514nm is shown, with a close-up of the E_{2g}^1 and A_{1g} regions, in Fig.3a (red curve). The frequency difference between E_{2g}^1 and A_{1g} and the FWHMs are preserved on PET, suggesting no degradation. The PL spectrum of 1L-MoS₂ on PET is shown in Fig.4b (red curve). The signal from 1L-MoS₂ is convolved within the background due to the PET substrate [Fig.4b (black curve)]. In order

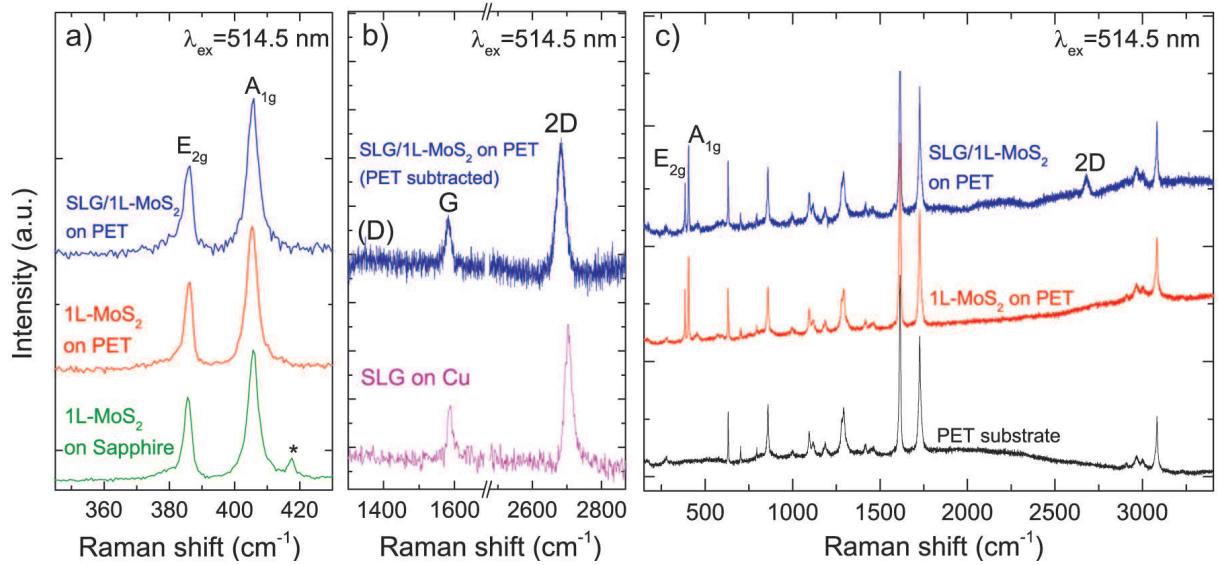


FIG. 3: (a) Raman spectra at 514nm for 1L-MoS₂ on sapphire, 1L-MoS₂ on PET, and SLG/1L-MoS₂. (b) Comparison at 514nm of the Raman spectra of as-grown SLG on Cu (magenta curve) with SLG/1L-MoS₂ after transfer on PET. (c) Raman spectra at 514nm of PET substrate (black curve), 1L-MoS₂ on PET (red curve) and SLG/1L-MoS₂ on PET (blue curve).

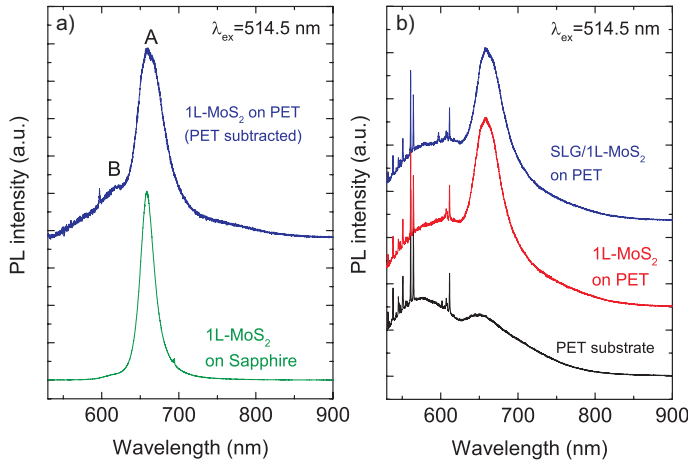


FIG. 4: (a) PL spectrum at 514nm (2.41eV) of 1L-MoS₂ on sapphire, and SLG/1L-MoS₂ after transfer on PET. (b) PL spectra of PET substrate (black curve), 1L-MoS₂ on PET (red curve) and SLG/1L-MoS₂ on PET (blue curve).

to reveal the underlying PL signature of 1L-MoS₂, we use a point-to-point subtraction between the spectrum of 1L-MoS₂ on PET [Fig.4b (red curve)] and the reference PET spectrum [Fig.4b (black curve)]. Prior to subtraction, the spectra are normalized to the intensity of the Raman peak at ~ 1615 cm^{-1} (corresponding to the peak at ~ 560 nm in Fig.4b), due to the stretching vibrations of benzene rings in PET[71]. As a result, the PL signal of 1L-MoS₂ can be seen in Fig.4a (blue curve) revealing no significant changes after transfer. The subsequent transfer of SLG on 1L-MoS₂ does not alter the 1L-MoS₂ PL position and lineshape [Fig.4b (blue curve)].

We then characterize the SLG transferred on 1L-MoS₂/PET. The intense Raman features of the underlying PET substrate[71] [Fig.3c (black curve)], mask the SLG peaks. In order to reveal the Raman signatures of SLG, we first measure the reference spectrum, shown in Fig.3c (black curve), of a PET substrate, using identical experimental conditions as those for SLG/1L-MoS₂/PET. We then implement a point-to-point subtraction, normalized to the intensity of the PET peak at ~ 1615 cm^{-1} , of the PET reference spectrum from the total spectrum Fig.3c (blue curve). The result is in Fig.3b (blue curve). The 2D peak retains its single-Lorentzian line-shape with $FWHM(2D) \sim 28$ cm^{-1} , validating the SLG transfer. The negligible D peak indicates that no significant defects are induced during transfer. $Pos(G) \sim 1584$ cm^{-1} , $FWHM(G) \sim 15$ cm^{-1} , $Pos(2D) \sim 2685$ cm^{-1} , $I(2D)/I(G) \sim 2.9$ and $A(2D)/A(G) \sim 5.9$, indicating a p-doping $\sim 3 \cdot 10^{12}$ cm^{-2} (~ 200 meV)[48, 68].

We then measure the absorption and transmission of SLG/1L-MoS₂ using a broadband (400-1300nm) white light from a tungsten halogen lamp. The transmitted light is collected by a 10x objective lens (NA=0.25) with a Horiba Jobin Yvon HR800 spectrometer equipped with a 300 grooves/mm grating, charged coupled device (CCD) detector and a 50 μm pinhole. Fig.5a plots the optical transmittance of bare PET (T_{PET} , black line), 1L-MoS₂ on PET (T_{MoS_2} , red line) and the final SLG/1L-MoS₂ stack on PET (T_{Hetero} , blue line) measured in the 400-800nm wavelength range. Fig.5b plots the absorption of 1L-MoS₂ on PET (Abs_{MoS_2} , red line) and of SLG/1L-MoS₂ on PET (Abs_{Hetero} , blue line), calculated as $Abs_{MoS_2} = (T_{PET} - T_{MoS_2}) / T_{PET}$ and $Abs_{Hetero} = (T_{PET} -$

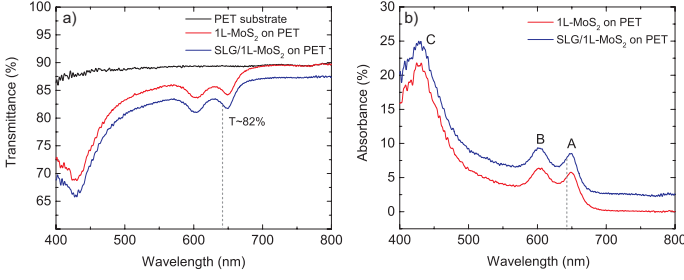


FIG. 5: (a) Transmittance of PET (black curve), 1L-MoS₂ on PET (red curve) and SLG/1L-MoS₂ on PET (blue curve). (b) Absorbance of 1L-MoS₂ and SLG/1L-MoS₂ as derived from the transmittance measurements. Dashed lines indicate our test wavelength.

T_{Hetero}/T_{PET} . The three peaks in Fig.5b at ~ 650 nm (1.91eV), ~ 603 nm (2.06eV), and ~ 428 nm (2.90eV) correspond to the A, B, C excitons of 1L-MoS₂[70, 72]. The positions of the A, B and C peaks remain unchanged after SLG transfer. The Abs difference between the two curves (red and blue) is $\sim 2.6\%$, consistent with the additional SLG absorption[73].

The PD area is shaped by etching, whereby SLG extending beyond the 1L-MoS₂ layer is removed in an oxygen plasma. The source-drain and gate electrodes are then defined by patterning the contacts area, followed by Cr/Au (6nm/60nm) evaporation and lift-off. PDs with different channels lengths (100 μ m-1mm), 2mm channel width and common side-gate electrodes (1cm x 0.5cm) are built, Fig.1b.

Refs.37,38 showed that the responsivity of SLG/MoS₂ PDs can be enhanced by gating. This induces a stronger electric field at the SLG/MoS₂ interface and promotes charge transfer. Various gating techniques have been exploited for GRM-based devices, including conventional Si/SiO₂ back-gates[74], high-k dielectrics (Al₂O₃, HfO₂)[75], chemical dopants[76], ionic liquids[77] and polymer electrolytes (PE)[48, 69]. In order to gate our SLG/1L-MoS₂ on PET, we employ the latter due to its compatibility with flexible substrates[78] and the ability to substantially dope SLG ($\pm 0.8eV$)[48, 69] using small gate voltages (up to 4V), unlike other gating techniques, which would require considerably higher biases to reach the same doping[74, 76]. We use a PE consisting of LiClO₄ and polyethylene oxide (POE)[48, 69]. We place the PE over both the SLG channel and the side-gate electrode, and use $-1V < V_{GS} < 1V$ in order to avoid electrochemical reactions, such as hydrolysis of residual water in the electrolyte[79, 80]. These reactions may permanently modify the SLG electrode[79, 80], and compromise the stability and performance of the device.

We characterize the responsivity at 642nm ($\sim 1.93eV$), slightly above the A exciton peak, where absorption of 1L-MoS₂ is maximized (Fig.5b). At 642nm the SLG/1L-MoS₂ heterostructure shows $\sim 8\%$ absorption (Fig.5b)

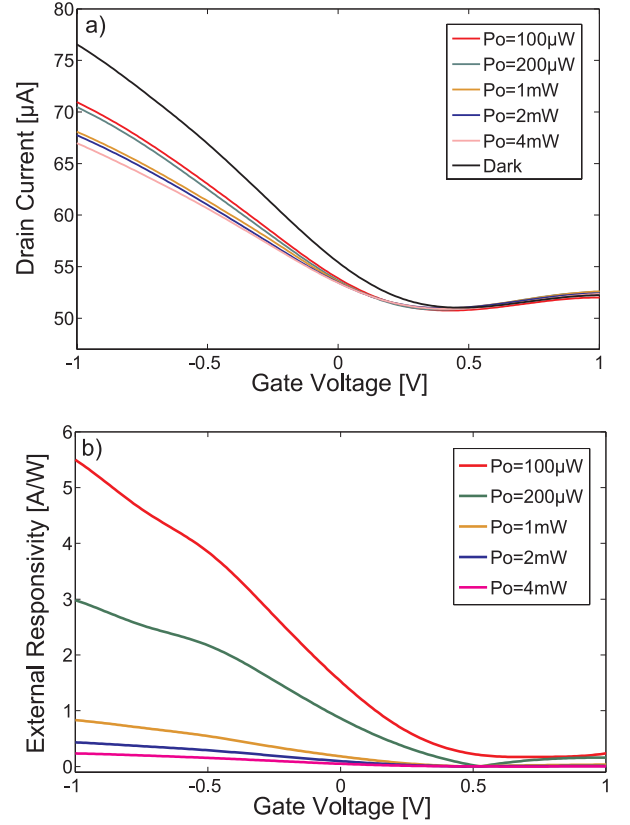


FIG. 6: a) Transfer characteristics as a function of P_o . b) R_{ext} as a function of V_{GS} and P_o . Channel length and width are 100 μ m and 2mm respectively.

and the device retains $\sim 82\%$ transparency (Fig.5a).

The $I_{DS} - V_{GS}$ measurements in Fig.6a are done at room temperature using a probe station and a parameter analyzer (Keithley 4200). The PD is illuminated at normal incidence by a collimated laser with P_o ranging from 100 μ W to 4mW. At these P_o and with $V_{DS} = 0.1V$ we measure a positive V_{CNP} ranging from $\sim 0.39V$ to $0.47V$, indicating an initial SLG p-doping $\sim 220meV$, consistent with the Raman estimate.

Fig.6a shows that, for $-1V < V_{GS} < 0.5V$ where SLG transport is hole dominated, the current decreases under illumination ($\sim 10\mu A$ at $V_{GS} = -1V$), as anticipated from the band-diagram of Fig.2. For $V_{GS} > 0.5V$, where SLG is electron-doped, the PD shows a small (up to $\sim 0.2\mu A$) current increase under illumination. Fig.6b plots R_{ext} as a function of V_{GS} , as derived from transconductance measurements using[19]:

$$R_{ext} = \frac{I_{light} - I_{dark}}{P_o \cdot A_{PD}/A_o} \quad (1)$$

where I_{light} and I_{dark} are the PD current under illumination and in dark, $I_{light} - I_{dark} = I_{ph}$, A_o is the laser spot area, A_{PD} is the PD area, and A_{PD}/A_o is a scaling factor that takes into account the fact that only a

fraction of optical power impinges the PD. As expected from the band-diagram in Fig.2, R_{ext} tends to increase for more negative V_{GS} , up to $\sim 5.5A/W$ at $V_{GS} = -1V$, $V_{DS} = 0.1V$ for $P_o = 100\mu W$. By taking into account that only 8% of light is absorbed ($P_{abs} = 0.08 \cdot P_o$), we derive $R_{int} = R_{ext}/0.08 = 69A/W$. Fig.6b implies that the higher P_o , the lower R_{ext} . This can be explained considering that the more photo-generated electrons are injected into the p-doped channel, the lower the electric field at the SLG/1L-MoS₂ interface, therefore a reduced injection of electrons causes R_{ext} to decrease.

Given that $R_{ext}, R_{int} > 1A/W$, we expect a photoconductive gain (G_{PD})[19, 81], whereby absorption of one photon results in multiple charge carriers contributing to I_{ph} . Our PDs act as optically-gated photoconductors, where the SLG conductance is modulated by optical absorption in the 1L-MoS₂. In this configuration, the presence of G_{PD} implies that the injected electrons in SLG can recirculate multiple times between source and drain, before recombining with trapped holes in 1L-MoS₂. Consequently, G_{PD} can be estimated as the ratio of electrons recombination (τ_{rec}) and transit (t_{tr}) times in the SLG channel: $G_{PD} = \tau_{rec}/t_{tr}$ [19, 21, 22, 81]. For higher V_{DS} , the free carriers drift velocity v_d in the SLG channel increases linearly with bias (Ohmic region) until it saturates, because of carriers scattering with optical phonons[82]. The linear increase in v_d results in shorter t_{tr} , i.e t_{tr} is defined as L/v_d , where L is the channel length[19, 21, 22, 81]. Therefore, G_{PD} is also expected to grow linearly with V_{DS} , providing higher R_{ext} . To confirm the photoconductive nature of G_{PD} in our device and test the dependence of R_{ext} on V_{DS} , we measure $I_{DS} - V_{DS}$ under illumination at $P_o = 100\mu W$ for $V_{GS} = -1V$ and calculate R_{ext} using Eq.1. We use $V_{DS} < 1V$ to keep the device operation in the linear (Ohmic) regime and minimize effect of non-linear dependence of v_d on V_{DS} (such as velocity saturation) that might appear for $V_{DS} > 1V$ [82]. As shown in Fig.7, R_{ext} scales with V_{DS} and reaches $\sim 45.5A/W$ ($R_{int} \sim 570A/W$) at $V_{DS} = 1V$. This is almost one order of magnitude higher than at $V_{DS} = 0.1V$, consistent with the similar increase in V_{DS} . These results are at least two orders of magnitude higher than semiconductor flexible membranes[4, 15] and five orders of magnitude larger than other flexible PDs based on GRMs[39, 40].

We define G_{PD} as the ratio between electrons recirculating in the SLG channel, thus sustaining I_{ph} , and the initial electron concentration injected into SLG from 1L-MoS₂[38]:

$$G_{PD} = \frac{I_{light} - I_{dark}}{q \cdot A_{PD} \cdot \Delta n_{ch}} \quad (2)$$

where q is the electron charge and Δn_{ch} is the concentration per unit area of the injected electrons. Δn_{ch} is equal to the trapped-hole concentration in 1L-MoS₂, which is related to charge neutrality point shift $\Delta V_{GS} = \Delta V_{CNP}$

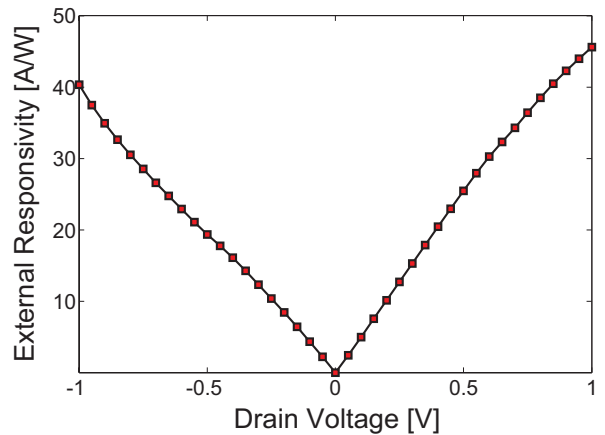


FIG. 7: R_{ext} as a function of V_{DS} for $P_o = 100\mu W$ at $V_{GS} = -1V$.

in the transfer characteristics. To calculate Δn_{ch} , we first write the potential balance in the metal-dielectric-SLG structure. When V_G is applied, it creates a gate-to-channel potential drop (V_{diel}), and it induces a local electrostatic potential in graphene channel ($V_{ch} = E_F/q$)[19, 48]:

$$V_G = V_{diel} + V_{ch} = \frac{Q_G}{C_G} + V_{ch} \quad (3)$$

where Q_G and C_G are the charge concentration and the geometrical capacitance per unit area associated with the gate electrode respectively. $|Q_G| = |q \cdot n_{ch}|$, reflecting the charge neutrality of the gate capacitor, with n_{ch} the charge carrier concentration per unit area in the channel. Any variations Δn_{ch} change ΔV_G . As a result:

$$\frac{dV_G}{dQ_G} = \frac{1}{C_G} + \frac{dV_{ch}}{dQ_G} \quad (4)$$

which leads to:

$$\Delta Q_G = (1/C_G + 1/C_Q)^{-1} \cdot \Delta V_G \quad (5)$$

where $C_Q = dQ_G/dV_{ch}$ is the SLG quantum capacitance[83, 84] that characterizes the changes of the channel potential ΔV_{ch} as a result of additional gating ΔQ_G , and $(1/C_G + 1/C_Q)^{-1}$ is the total capacitance C_{tot} .

To calculate Q_G we first need to find C_G and C_Q . In PE gating, C_G is associated with the EDL at the SLG/electrolyte interface[48, 83, 85, 86]. The EDL acts like a parallel-plate capacitor with an dielectric layer thickness of the order of λ_D , so that $C_G = C_{EDL} = \epsilon \epsilon_0 / \lambda_D$, where ϵ is the PE dielectric constant, and ϵ_0 is the vacuum permittivity. In principle, for a monovalent electrolyte, λ_D can be explicitly calculated[87] if the electrolyte concentration is known. However, in the presence of a polymer matrix, the electrolyte ions can form complexes with polymer chains[88], therefore the precise ion

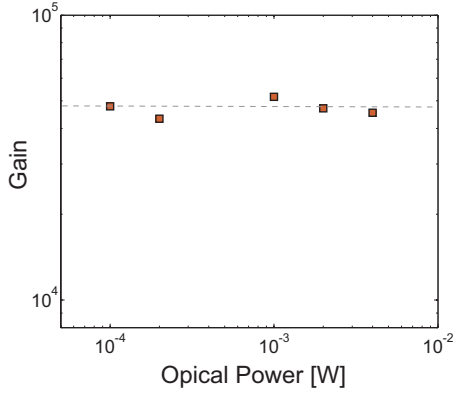


FIG. 8: G_{PD} as a function of P_o at $V_{GS} = -1V$ and $V_{DS} = 0.1V$.

concentration is difficult to measure. For PE gating, different EDL thicknesses in the range $\sim 1 - 5nm$ have been reported[48, 49, 85, 86]. To estimate C_{EDL} in our devices we take $\lambda_D \sim 2nm$ [48] and the dielectric constant of the PEO matrix to be $\epsilon \sim 5$ [89], as done in Ref.48. As a result, we obtain $C_{EDL} = 2.2 \times 10^{-6} F/cm^2$. This is the same order of magnitude as the SLG C_Q [83]. Therefore the latter cannot be neglected in Eq.5. C_Q is given by[83]:

$$C_Q \approx \frac{2q^2}{\hbar v_F \sqrt{\pi}} \cdot \sqrt{n_{ch} + n_i} \quad (6)$$

where \hbar is the reduced Planck constant, $v_F = 1.1 \cdot 10^6 m/s$ is the Fermi velocity of charge carriers in graphene[74, 90] and n_i is the intrinsic carrier concentration in SLG near the Dirac point induced by charge impurities, defects and local potential fluctuations in the SLG channel[83, 91–93]. Using Raman and transconductance we estimate $n_i \sim 3 \cdot 10^{12} cm^{-2}$. From Eq.6 we then get $C_Q = 4 \cdot 10^{-6} F/cm^2$ at V_{CNP} . From Fig.6a, and extracting ΔV_{CNP} between the dark current and the transfer curves measured under illumination, and with Eq.5, we get Δn_{ch} ranging from $4 - 8 \cdot 10^{11} cm^{-2}$ for P_o going from $100\mu W$ to $4mW$. As a result, we obtain $G_{PD} \sim 5 \times 10^4$ at $V_{DS} = 0.1V$ for different P_o as shown in Fig.8. As discussed previously, G_{PD} becomes larger for higher V_{DS} . Thus, we measure an increase of almost order of magnitude ($G_{PD} \sim 4 \cdot 10^5$ at $P_o = 100\mu W$) for V_{DS} going from 0.1V to 1V.

Finally, we test I_{ph} as a function of bending. r_b is estimated as $(h^2 + (l/2)^2)/2h$, where l is the chord of circumference connecting the two ends of the arc, and h is the height at the chord midpoint. Fig.9b plots I_{ph} for different r_b , showing a maximal deviation of 15% for r_b down to 6cm. This value is comparable to r_b reported for semiconductor membrane PDs[4, 15], yet the latter show two orders of magnitude lower ($< 0.3A/W$) responsivities[4, 15]. Although our r_b is one order of magnitude larger than reported by flexible single NW

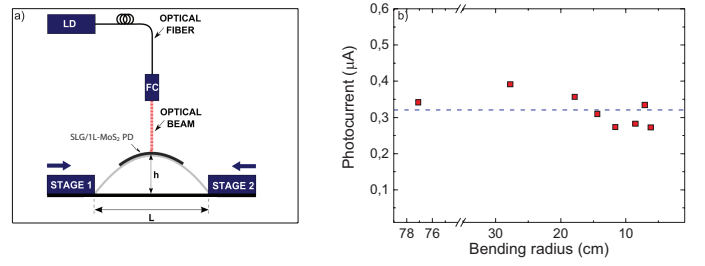


FIG. 9: a) Schematic two-points bending setup. LD = laser diode; FC= fiber collimator; b) I_{ph} as a function of r_b . The dashed line shows the mean value.

devices[3, 16–18], the device area of our PDs ($> 0.2mm^2$) is at least four orders of magnitude larger compared to these devices ($< 5\mu m^2$).

Conclusions

We reported flexible PDs for visible wavelengths with external responsivity up to $\sim 45.5A/W$ and photoconductive gain of 4×10^5 . This is at least two orders of magnitude higher than semiconductor flexible membranes and other GRM-based flexible PDs reported thus far. Our PDs show stable performance upon bending for radii of curvature larger than $\sim 6cm$. The responsivity, flexibility, transparency and low operation voltage (below 1V) of our PDs makes them attractive candidates for wearable, biomedical and low-power opto-electronic applications.

We acknowledge funding from EU Graphene Flagship (no. 604391), ERC Grant Hetero2D, EPSRC Grants EP/K01711X/1, EP/K017144/1, EU grant GENIUS, a Royal Society Wolfson Research Merit Award

* Electronic address: acf26@eng.cam.ac.uk

- [1] Akinwande, D., Petrone, N., Hone, J. *Nat. Commun.* **2014**, 5.
- [2] Ryhaenen, T. T., **2010**, Cambridge University Press.
- [3] Liu, Z., Chen, G., Liang, B., Yu, G., Huang, H., Chen, D., Shen, G. *Opt. Express* **2013**, 21, 7799-7810.
- [4] Yuan, H.-C., Shin, J., Qin, G., Sun, L., Bhattacharya, P., Lagally, M. G., Celler, G. K., Ma, Z. *Appl. Phys. Lett.* **2009**, 94, 13102.
- [5] Park, S.-I., Xiong, Y., Kim, R.-H., Elvikis, P., Meitl, M., Kim, D.-H., Wu, J., Yoon, J., Yu, C.-J., Liu, Z., et al. *Science* **2009**, 325, 977-981.
- [6] Qiang, Z., Yang, H., Chen, L., Pang, H., Ma, Z., Zhou, W. *App. Phys. Lett.* **2008**, 93, 061106.
- [7] Bosman, E., Van Steenberge, G., Van Hoe, B., Missinne, J., Vanfleteren, J., Van Daele, P. *Photon. Technol. Lett., IEEE* **2010**, 22, 287-289.
- [8] Chen, Z., Ren, W., Gao, L., Liu, B., Pei, S., Cheng, H.-M. *Nat. Mater.* **2011**, 10, 424-428.
- [9] Shahi, S. *Nature Photon.* **2010**, 4, 506-506.

- [10] Yoon, J., Li, L., Semichaevsky, A. V., Ryu, J. H., Johnson, H. T., Nuzzo, R. G., Rogers, J. A. *Nat. Commun.* **2011**, *2*, 343.
- [11] Kim, D.-H., Lu, N., Ma, R., Kim, Y.-S., Kim, R.-H., Wang, S., Wu, J., Won, S. M., Tao, H., Islam, A., et al. *Science* **2011**, *333*, 838-843.
- [12] Ko, H. C., Stoykovich, M. P., Song, J., Malyarchuk, V., Choi, W. M., Yu, C.-J., Geddes Iii, J. B., Xiao, J., Wang, S., Huang, Y., et al. *Nature* **2008**, *454*, 748-753.
- [13] Blakemore, J. S. *J. Appl. Phys.* **1982**, *53*, 123-181.
- [14] MacMillan, N. H. *J. Mater. Sci.* **1972**, *7*, 239-254.
- [15] Yang, W., Yang, H., Qin, G., Ma, Z., Berggren, J., Hammar, M., Soref, R., Zhou, W. *Appl. Phys. Lett.* **2010**, *96*, 121107.
- [16] Chen, G., Liang, B., Liu, Z., Yu, G., Xie, X., Luo, T., Xie, Z., Chen, D., Zhu, M.-Q., Shen, G. *J. Mater. Chem. C* **2014**, *2*, 1270-1277.
- [17] Lee, S., Jung, S. W., Park, S., Ahn, J., Hong, S. J., Yoo, H. J., Lee, M. H., Cho, D. I. *Proc. IEEE Micr. Elect.*, **2012**.
- [18] Yu, G., Liu, Z., Xie, X., Ouyang, X., Shen, G. *J. Mater. Chem. C* **2014**, *2*, 6104-6110.
- [19] Sze, S. M., Kwok, K. N. **2006**, Wiley, New York.
- [20] Bonaccorso, F., Sun, Z., Hasan, T., Ferrari, A. C. *Nature Photon.* **2010**, *4*, 611-622.
- [21] Ferrari, A. C., Bonaccorso, F., Fal'ko, V., Novoselov, K. S., Roche, S., Boggild, P., Borini, S., Koppens, F. H. L., Palermo, V., Pugno, N., et al. *Nanoscale* **2015**, *7*, 4598-4810.
- [22] Koppens, F. H. L., Mueller, T., Avouris, P., Ferrari, A. C., Vitiello, M. S., Polini, M. *Nat. Nanotechnol.* **2014**, *9*, 780-793.
- [23] Sun, Z. P., Hasan, T., Torrisi, F., Popa, D., Privitera, G., Wang, F. Q., Bonaccorso, F., Basko, D. M., Ferrari, A. C. *Acs Nano* **2010**, *4*, 803-810.
- [24] Kim, K. S., Zhao, Y., Jang, H., Lee, S. Y., Kim, J. M., Kim, K. S., Ahn, J.-H., Kim, P., Choi, J.-Y., Hong, B. H. *Nature* **2009**, *457*, 706-710.
- [25] Baugher, B. W. H., Churchill, H. O. H., Yang, Y., Jarillo-Herrero, P. *Nat. Nanotechnol.* **2014**, *9*, 262-267.
- [26] Pospischil, A., Furchi, M. M., Mueller, T. *Nat. Nanotechnol.* **2014**, *9*, 257-261.
- [27] Lopez-Sanchez, O.; Lembke, D.; Kayci, M.; Radenovic, A.; Kis, A. *Nat. Nanotechnol.* **2013**, *8*, 497-501.
- [28] Xia, F.; Mueller, T.; Lin, Y. M.; Valdes-Garcia, A.; Avouris, P. *Nat. Nanotechnol.* **2009**, *4*, 839-843.
- [29] Liu, M., Yin, X. B., Ulin-Avila, E., Geng, B. S., Zentgraf, T., Ju, L., Wang, F., Zhang, X. *Nature* **2011**, *474*, 64-67.
- [30] Chen, J., Badioli, M., Alonso-Gonzalez, P., Thongratanasiri, S., Huth, F., Osmond, J., Spasenovic, M., Centeno, A., Pesquera, A., Godignon, P., et al. *Nature* **2012**, *487*, 77-81.
- [31] Echtermeyer, T. J., Britnell, L., Jasnós, P. K., Lombardo, A., Gorbachev, R. V., Grigorenko, A. N., Geim, A. K., Ferrari, A. C., Novoselov, K. S. *Nat. Commun.* **2011**, *2*, 458.
- [32] Fei, Z., Rodin, A. S., Andreev, G. O., Bao, W., McLeod, A. S., Wagner, M., Zhang, L. M., Zhao, Z., Thiemens, M., Dominguez, G., et al. *Nature* **2012**, *487*, 82-85.
- [33] Ju, L., Geng, B., Horng, J., Girit, C., Martin, M., Hao, Z., Bechtel, H. A., Liang, X., Zettl, A., Shen, Y. R., et al. *Nat. Nanotechnol.* **2011**, *6*, 630-634.
- [34] Yan, H., Li, X., Chandra, B., Tulevski, G., Wu, Y., Freitag, M., Zhu, W., Avouris, P., Xia, F. *Nat. Nanotechnol.* **2012**, *7*, 330-334.
- [35] Furchi, M. M., Pospischil, A., Libisch, F., Burgdrfer, J., Mueller, T. *Nano Lett.* **2014**, *14*, 4785-4791.
- [36] Withers, F., Del Pozo-Zamudio, O., Mishchenko, A., Rooney, A. P., Gholinia, A., Watanabe, K., Taniguchi, T., Haigh, S. J., Geim, A. K., Tartakovskii, A. I., et al. *Nat. Mater.* **2015**, *14*, 301-306.
- [37] Roy, K., Padmanabhan, M., Goswami, S., Sai, T. P., Ramalingam, G., Raghavan, S., Ghosh, A. *Nat. Nanotechnol.* **2013**, *8*, 826-830.
- [38] Zhang, W. J., Chuu, C. P., Huang, J. K., Chen, C. H., Tsai, M. L., Chang, Y. H., Liang, C. T., Chen, Y. Z., Chueh, Y. L., He, J. H., et al. *Sci. Rep.* **2014**, *4*.
- [39] Finn, D. J., Lotya, M., Cunningham, G., Smith, R. J., McCloskey, D., Donegan, J. F., Coleman, J. N. *J. Mater. Chem. C* **2014**, *2*, 925-932.
- [40] Withers, F., Yang, H., Britnell, L., Rooney, A. P., Lewis, E., Felten, A., Woods, C. R., Romaguera, V. S., Georgiou, T., Eckmann, A., et al. *Nano Lett.* **2014**, *14*, 3987-3992.
- [41] Bonaccorso, F., Lombardo, A., Hasan, T., Sun, Z. P., Colombo, L., Ferrari, A. C. *Mater. Today* **2012**, *15*, 564-589.
- [42] Hernandez, Y., Nicolosi, V., Lotya, M., Blighe, F. M., Sun, Z. Y., De, S., McGovern, I. T., Holland, B., Byrne, M., Gun'ko, Y. K. et al. *Nat. Nanotechnol.* **2008**, *3*, 563-568.
- [43] King, P. J., Khan, U., Lotya, M., De, S., Coleman, J. N. *Acs Nano* **2010**, *4*, 4238-4246.
- [44] Torrisi, F., Coleman, J. N. *Nat. Nanotechnol.* **2014**, *9*, 738-739.
- [45] Faraj, M. G., Ibrahim, K., Ali, M. K. M. *Optoelectron Adv. Mat.* **2011**, *5*, 879-882.
- [46] Martins, L. G. P., Song, Y., Zeng, T. Y., Dresselhaus, M. S., Kong, J., Araujo, P. T. *Proc. Natl Acad. Sci. USA* **2013**, *110*, 17762-17767.
- [47] Bae, S., Kim, H., Lee, Y., Xu, X., Park, J. S., Zheng, Y., Balakrishnan, J., Lei, T., Kim, H. R., Song, Y. I., et al. *Nat. Nanotechnol.* **2010**, *5*, 574-8.
- [48] Das, A., Pisana, S., Chakraborty, B., Piscanec, S., Saha, S. K., Waghmare, U. V., Novoselov, K. S., Krishnamurthy, H. R., Geim, A. K., Ferrari, A. C., Sood, A. K. *Nat. Nanotechnol.* **2008**, *3*, 210-5.
- [49] Das, A., Chakraborty, B., Piscanec, S., Pisana, S., Sood, A. K., Ferrari, A. C. *Phys. Rev. B* **2009**, *79*, 155417.
- [50] Choi, M. S., Lee, G. H., Yu, Y. J., Lee, D. Y., Lee, S. H., Kim, P., Hone, J., Yoo, W. J., *Nat. Commun.* **2013**, *4*, 1624.
- [51] Das, S., Chen, H. Y., Penumatcha, A. V., Appenzeller, J., *Nano Lett.* **2013**, *13*, 100-105.
- [52] Shan, B., Cho, K. *Phys. Rev. Lett.* **2005**, *94*, 236602.
- [53] Yu, Y.-J., Zhao, Y., Ryu, S., Brus, L. E., Kim, K. S., Kim, P. *Nano Lett.* **2009**, *9*, 3430-3434.
- [54] Kim, B. J., Jang, H., Lee, S.-K., Hong, B. H., Ahn, J.-H., Cho, J. H. *Nano Lett.* **2010**, *10*, 3464-3466.
- [55] Lee, S. K., Jang, H. Y., Jang, S., Choi, E., Hong, B. H., Lee, J., Park, S., Ahn, J. H. *Nano Lett.* **2012**, *12*, 3472-3476.
- [56] Dumcenco, D., Ovchinnikov, D., Marinov, K., Lazic, P., Gibertini, M., Marzari, N., Sanchez, O. L., Kung, Y.-C., Krasnozhon, D., Chen, M.-W. et al. *Acs Nano* **2015**, *9*, 4611-4620.
- [57] Li, X. S., Cai, W. W., An, J. H., Kim, S., Nah, J., Yang, D. X., Piner, R., Velamakanni, A., Jung, I., Tutuc, E.,

- et al. *Science* **2009**, *324*, 1312-1314.
- [58] Verble, J. L., Wieting, T. J. *Phys. Rev. Lett.* **1970**, *25*, 362-365.
- [59] Wieting, T. J., Verble, J. L. *Phys. Rev. B* **1971**, *3*, 4286-4292.
- [60] Lee, C., Yan, H. G., Brus, L. E., Heinz, T. F., Hone, J., Ryu, S. *Acs Nano* **2010**, *4*, 2695-2700.
- [61] Li, H., Zhang, Q., Yap, C. C. R., Tay, B. K., Edwin, T. H. T., Olivier, A., Baillargeat, D. *Adv. Funct. Mater.* **2012**, *22*, 1385-1390.
- [62] Porto, S. P. S., Krishnan, R. S. *J. Chem. Phys.* **1967**, *47*, 1009-1012.
- [63] Lagatsky, A. A., Sun, Z., Kulmala, T. S., Sundaram, R. S., Milana, S., Torrisi, F., Antipov, O. L., Lee, Y., Ahn, J. H., Brown, C. T. A., et al. *Appl. Phys. Lett.* **2013**, *102*, 013113.
- [64] Ferrari, A. C., Meyer, J. C., Scardaci, V., Casiraghi, C., Lazzeri, M., Mauri, F., Piscanec, S., Jiang, D., Novoselov, K. S., Roth, S., et al. *Phys. Rev. Lett.* **2006**, *97*, 187401.
- [65] Cancado, L. G., Jorio, A., Ferreira, E. H., Stavale, F., Achete, C. A., Capaz, R. B., Moutinho, M. V., Lombardo, A., Kulmala, T. S., Ferrari, A. C. *Nano Lett.* **2011**, *11*, 3190-6.
- [66] Ferrari, A. C., Basko, D. M. *Nat. Nanotechnol.* **2013**, *8*, 235-46.
- [67] Ferrari, A. C., Robertson, J. *Phys. Rev. B* **2000**, *61*, 14095-14107.
- [68] Basko, D. M., Piscanec, S., Ferrari, A. C. *Phys. Rev. B* **2009**, *80*, 165413.
- [69] Bruna, M., Ott, A. K., Ijas, M., Yoon, D., Sassi, U., Ferrari, A. C. *Acs Nano* **2014**, *8*, 7432-7441.
- [70] Mak, K. F., Lee, C., Hone, J., Shan, J., Heinz, T. F. *Phys. Rev. Lett.* **2010**, *105*, 136805.
- [71] Boerio, F. J., Bahl, S. K., McGraw, G. E. *J. Poly. Sci.* **1976**, *14*, 1029-1046.
- [72] Qiu, D. Y., da Jornada, F. H., Louie, S. G. *Phys. Rev. Lett.* **2013**, *111*, 216805.
- [73] Nair, R. R., Blake, P., Grigorenko, A. N., Novoselov, K. S., Booth, T. J., Stauber, T., Peres, N. M. R., Geim, A. K. *Science* **2008**, *320*, 1308-1308.
- [74] Novoselov, K. S., Geim, A. K., Morozov, S. V., Jiang, D., Katsnelson, M. I., Grigorieva, I. V., Dubonos, S. V., Firsov, A. A. *Nature* **2005**, *438*, 197-200.
- [75] Lemme, M. C., Echtermeyer, T. J., Baus, M., Kurz, H. *IEEE Electr. Device L.* **2007**, *28*, 282-284.
- [76] Wehling, T. O., Novoselov, K. S., Morozov, S. V., Vdovin, E. E., Katsnelson, M. I., Geim, A. K., Lichtenstein, A. I. *Nano Lett.* **2008**, *8*, 173-177.
- [77] Ye, J. T., Craciun, M. F., Koshino, M., Russo, S., Inoue, S., Yuan, H. T., Shimotani, H., Morpurgo, A. F., Iwasa, Y. *Proc. Natl Acad. Sci. USA* **2011**, *108*, 13002-13006.
- [78] Sirringhaus, H., Kawase, T., Friend, R. H., Shimoda, T., Inbasekaran, M., Wu, W., Woo, E. P. *Science* **2000**, *290*, 2123-2126.
- [79] Azais, P., Duclaux, L., Florian, P., Massiot, D., Lillo-Rodenas, M.-A., Linares-Solano, A., Peres, J.-P., Jehoulet, C., Bguin, F. *J. Power Sources* **2007**, *171*, 1046-1053.
- [80] Efetov, D. K., Kim, P. *Phys. Rev. Lett.* **2010**, *105*, 256805.
- [81] Konstantatos, G., Badioli, M., Gaudreau, L., Osmond, J., Bernechea, M., de Arquer, G., Gatti, F., Koppens, F. H. L. *Nat. Nanotechnol.* **2012**, *7*, 363-368.
- [82] Meric, I., Han, M. Y., Young, A. F., Ozyilmaz, B., Kim, P., Shepard, K. L. *Nat. Nanotechnol.* **2008**, *3*, 654-659.
- [83] Xia, J., Chen, F., Li, J., Tao, N. *Nat. Nanotechnol.* **2009**, *4*, 505-509.
- [84] Fang, T., Konar, A., Xing, H., Jena, D. *Appl. Phys. Lett.* **2007**, *9*, 092109.
- [85] Ozel, T., Gaur, A., Rogers, J. A., Shim, M. *Nano Lett.* **2005**, *5*, 905-911.
- [86] Lu, C., Fu, Q., Huang, S., Liu, J. *Nano Lett.* **2004**, *4*, 623-627.
- [87] Russel, W.B., Saville, D.A. and Schowalter, W. R. **1989**, Cambridge University Press, UK.
- [88] Salomon, M., Xu, M., Eyring, E. M., Petrucci, S. *J. Phys. Chem.* **1994**, *98*, 82348244.
- [89] Boyd, R. H. *J. Polym. Sci. Polym. Phys.* **1983**, *21*, 505514.
- [90] Zhang, Y. B., Tan, Y. W., Stormer, H. L., Kim, P. *Nature* **2005**, *438*, 201-204.
- [91] Adam, S., Hwang, E. H., Galitski, V. M., Sarma, S. D. *Proc. Natl. Acad. Sci. USA* **2007**, *104*, 18392-18397.
- [92] Chen, J. H., Jang, C., Adam, S., Fuhrer, M. S., Williams, E. D., Ishigami, M. *Nature Phys.* **2008**, *4*, 377-381.
- [93] Victor, M. G., Shaffique, A., Sarma, S. D. *Phys. Rev. B* **2007**, *76*, 245405.